Planar Solid-State Nanopores Toward Scalable Nanofluidic Integration Based on CMOS Technology

Advanced Engineering Materials

ADVANCED ENGINEERING MATERIALS
www.aem-journal.com

RESEARCH ARTICLE OPEN ACCESS

Planar Solid-State Nanopores Toward Scalable Nanofluidic Integration Based on CMOS Technology

Ngan Hoang Pham[1] | Chenyu Wen[1] | Mohammad Hadi Khaksaran[1,2] | Won-Yong Lee[1,3] | Javier Cruz[4,5] | Klas Hjort[4] | Dongping Wu[6] | Shi-Li Zhang[1]

[1]Division of Solid-State Electronics, Department of Electrical Engineering, Uppsala University, Uppsala, Sweden | [2]Department of Microtechnology and Nanoscience, Chalmers University of Technology, Gothenburg, Sweden | [3]Department of Physics, Chung-Ang University, Seoul Republic of Korea | [4]Division of Microsystems Technology, Department of Materials Science and Engineering, Uppsala University, Uppsala, Sweden | [5]ienai SPACE, Leganés, Spain | [6]School of Microelectronics, Fudan University, Shanghai, China

Correspondence: Shi-Li Zhang (shili.zhang@angstrom.uu.se)

Received: 21 July 2025 | **Revised:** 10 April 2026 | **Accepted:** 10 April 2026

Keywords: ionic transport | nanofluidic integration | planar solid-state nanopores | silicon technology | streaming current

ABSTRACT

Solid-state nanopores (SSNPs) are of potential for a wide range of applications from single-molecule detection and selective filtration to osmotic power harvesting and iontronics. As the demand for such applications escalates, a design scheme to sophisticate the nanopore platform is to integrate complementary nanofluidic components, including nanochannels and nanoreactors, to realize fully fletched lab-on-chip systems. Herein, we present a scalable fabrication strategy for planar SSNPs based on standard silicon technology that has been developed for advanced integrated circuits. We demonstrate a prototype device featuring a nanopore linking two microfluidic reservoirs, characterize its electrical noise profile, and quantify the streaming current generated under a pressure-driven flow. Use of the silicon nanofabrication process further allows the geometry and dimension (length, width, height) of each planar nanopore to be independently designed and the nanopores to naturally become part of a fluidic system with mixed micro- and nanoscale channels on the same chip. This process supports wafer-scale manufacture of high-density micro/nanofluidics, delivers exceptional mechanical stability, and is fully compatible with complementary metal-oxide-semiconductor electronics. Together, these attributes establish a versatile, integrable nanofluidic platform for next-generation sensing, energy, and analytical applications.

1 | Introduction

A nanopore is a nanometer-scale aperture that connects two fluidic reservoirs filled with electrolytes. When an electric field is applied across the nanopore, it induces ionic transport, resulting in an appreciable ionic current [1]. Transport of ions and water molecules through such a nanopore is a fundamental process that governs the functionality and performance of nanopore-based devices. Unlike transport in macroscopic systems, ions and solvent dynamics within nanoscale confinements are dominated by their strong interactions with the pore surface. Parameters, such as surface charge density, wettability, surface dipole moments, and nanoscale roughness, critically affect these interactions [1]. Such microscopic details constitute the basis for a rich array of highly coupled, nonlinear, and nonequilibrium behaviors including ionic concentration polarization [1], current rectification [2], induced-charge electrokinetic effects [3], electroosmotic flow [4], and blue energy (osmotic power) generation [5]. Leveraging ion-transport behavior of nanopore platforms has been developed for diverse technological applications including neuromorphic circuits [6–8] and iontronic transistors [9].

Ngan Hoang Pham and Chenyu Wen are cofirst authors.

Solid-state nanopores (SSNPs) are usually fabricated in synthetic membranes composed of materials like silicon [10–12], silicon nitride (SiN_x), silicon dioxide (SiO_2), graphene, and transition metal dichalcogenides (e.g., MoS_2 and WS_2) [1, 13]. The SSNPs offer greater mechanical robustness, chemical stability, and tunability in size and geometry than what their counterpart biological nanopores do. Conventional SSNPs are typically vertical in configuration by drilling through freestanding membranes using ion beam or electron beam, anisotropic chemical etching, ion-track etching, metal-assisted chemical etching [1, 13–15], and a combination of lithography and reactive ion etching (RIE) [1]. Pore diameters achieved with these methods range from subnanometers to hundreds of nanometers.

Despite their ease in fabrication, the conventional vertical configuration imposes severe limitations. The same substrate needs to perform two functions at the same time: the pore-hosting carrier and the mechanical support for pore formation. The challenge is that the latter continually erodes the former when the nanopore density increases. Making micro-/nano-channels to realize an ionic circuit with such vertical nanopores is largely incompatible with standard silicon (Si) technology. Furthermore, vertical systems offer limited control over pore shape, with geometries often restricted to a few options due to the constraints of etching processes. Precise tuning of sidewall inclination angles and surface curvature remains a significant challenge, yet emerging evidence shows that the nanopore geometry plays a critical role in ionic rectification and analyte transport dynamics [10, 11, 16].

To meet these challenges, a new configuration with planar or in-plane nanopores has gained increasing attention [17–19]. With this configuration, nanopores are patterned laterally within the same plane as the fluidic pathway, enabling a serial arrangement of multiple sensing elements. This in-plane design offers key benefits with improved integration with auxiliary nanofluidic elements (e.g., mixers, separators, reactors), simplified device assembly, and enhanced compatibility with orthogonal detection methods such as optical readouts [17, 19]. Additionally, serial nanopore arrays improve sensing precision by enabling signal averaging across multiple detection sites, thereby reducing variability and enhancing analyte discrimination [18]. Several fabrication methods have been proposed for constructing such planar nanopores. Among them, focused ion beam (FIB) milling stands out for its ability to precisely sculpt in-plane nanostructures [17]. For instance, a glass-based nanopore device incorporating two to eight in-plane nanopores in series for real-time resistive-pulse sensing of viral capsids has been reported [17]; an increased pore number leads to reduced pulse variability and improved detection precision. Similarly, serial in-plane nanopores have been utilized to enhance signal fidelity in single-molecule analysis [18]. However, the FIB-based fabrication strategy suffers from throughput, alignment accuracy, reproducibility or uniformity, and compatibility with scalable manufacturing techniques. It is labor intensive and requires high-end equipment, which limits widespread adoption. Addressing these drawbacks remains a critical step toward a broader deployment of planar nanopore technologies in integrated nanofluidic systems.

In the present work, we report a robust and scalable fabrication strategy for planar SSNPs (pSSNPs) based on standard Si nanofabrication process technology developed for advanced integrated circuits. Once the pSSNPs connected to their respective microfluidic reservoirs are produced using electron beam lithography (EBL) and RIE, anodic bonding is applied to seal the fluidic channels. The pSSNPs are both imaged using electron microscope and electrically analyzed in terms of current–voltage (I–V) characteristics, noise performance, and streaming current. Through detailed experimental analysis, we have established a generalized noise model for pSSNPs. This model not only captures the key features observed in our measurements but also provides a predictive framework for evaluating noise behavior in even smaller nanopores that are currently beyond experimental reach. Our approach enables precise definition of nanopore geometry in terms of size (length, width, and height), shape, and degree of asymmetry, within the same nanofluidic plane. The process supports the integration of multiple nanopores with independently controlled designs on a single substrate, allowing for their strategic placement and serial alignment. Such configurations enable sequential signal acquisition from analytes under continuous flow, opening up new possibilities for multiplexed sensing and high-resolution signal deconvolution. Beyond sensor integration, this platform offers significant potential for developing nanofluidic logic circuits, programmable ionic systems, and miniaturized fluidic computation architectures, marking a step forward toward the next-generation multifunctional nanofluidic chips.

2 | Experimental Section

Fabrication of the pSSNPs involves both Si processing and anodic wafer bonding. Characterization of the fabricated devices concerns both microscope imaging and electrical measurements. As both parts are substantial, they are described in subsections below.

2.1 | Fabrication of Planar Nanopores

Although the fabrication method allows for the definition of nanopores with varying dimensions, we focus in this work exclusively on pSSNPs 60 nm in length with a cross-section nominally 50 nm in width and 50 nm in height, oriented laterally with respect to the substrate surface.

By referring to Figure 1, the pSSNP devices were fabricated on single-side polished (100) Si wafers of 525 μm in thickness. Following standard cleaning protocols, the fabrication began with the definition of alignment marks for EBL (nB5, NanoBeam Ltd.). Silicon oxide nanowires 50 nm wide and 50 nm tall were generated by exposing a negative-tone hydrogen silsesquioxane (HSQ) resist (Step 1). A 450 nm-thick amorphous Si layer was then deposited via low-pressure chemical vapor deposition (ExperTech CTR-200 Compact Thermal Reactor) to minimize topographic variations over the nanopore region (Step 2). While these oxide nanowire dimensions determine the nanopore width and height, the length of the nanopores is defined during reactively ion etching (Applied Materials Precision 5000 Mark II) the microfluidic reservoirs connected to them (Step 3). A vertical sidewall profile was essential at this

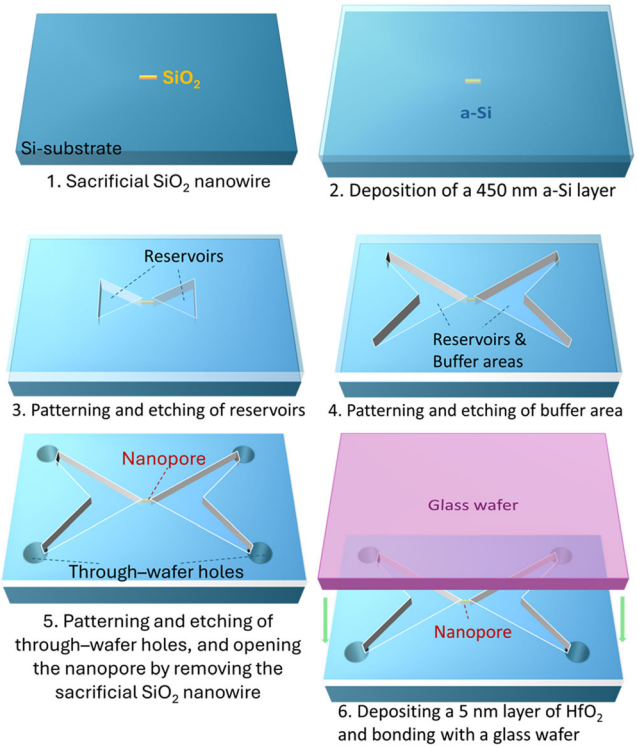

FIGURE 1 | Process flow for the fabrication of our planar SSNPs. SSNPs = Solid-state nanopores.

stage to preserve the nanopore structure between the reservoirs, necessitating the use of suitable etching chemistry. Intermediate buffer regions of 10 µm depth were also created to mitigate capillary effects and ensure controlled fluid delivery (Step 4), prior to the formation of through-wafer access holes (250 µm in diameter) etched in the Si substrate using deep RIE (Tegal 110 S/DE) (Step 5). The pSSNPs were subsequently opened by selectively removing the sacrificial oxide nanowires using buffered hydrofluoric acid (BHF). To enhance surface wettability and ensure stable electrolyte interaction, a thin layer (≤5 nm) of hafnium oxide (HfO_2) was deposited via atomic layer deposition (ALD) (Picosun R-200 ALD Unit) [20]. This ALD step would lead to a reduction of the nanopore width and height as well as an increase of the length all by about 10 nm (i.e., twice the HfO_2 thickness). Finally, the nanopores along with their respective microfluidic reservoirs were enclosed by bonding the patterned Si wafer to a borosilicate glass substrate using anodic bonding at 380°C, under a 950 V bias for 24 h (Step 6).

2.2 | Characterization and Data Processing

A particularly nontrivial step in the fabrication process is the reliable sealing of the pSSNPs along with their microfluidic reservoirs (Figure 2a). A successful implementation of anodic bonding allows for a robust enclosure, enabling electrochemical characterization of well-defined pSSNPs on a customized four-terminal, multi-inlet–outlet setup fabricated using 3D printing (Figure 2b and Supporting Information [SI]). Before each electrical measurement, the chips were thoroughly cleaned and rinsed in deionized water (DIW). The inlets and outlets were then inserted with electrolytes via the through-wafer access holes. The four terminals each with its own Ag/AgCl electrode were freshly made before measurement by chlorinating Ag wires using household bleach [21]. This configuration with the electrodes represents a typical four-point probe setup to eliminate the effect of parasitic contact and series resistances when extracting the conductance of the nanopore from the *I–V* curves acquired by applying a bias voltage between two electrodes while measuring the ionic current between two other electrodes. An added

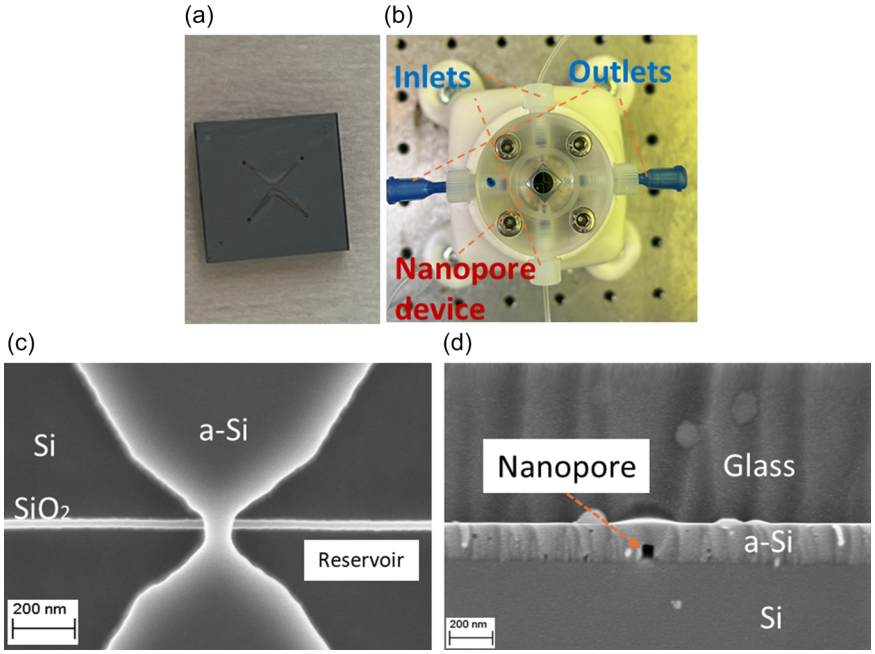

FIGURE 2 | (a) A completed pSSNP device 10 mm × 10 mm in size, (b) top view of the customized measurement cell with a pSSNP device loaded as well as the inlets, outlets, and electrodes, (c) top view of the sacrificial SiO_2 nanowire for pore formation and the two reservoirs, and (d) cross section, side, view of the pSSNP after removal of the SiO_2 nanowire and the wafer bonding (Figure 1, Step 6). pSSNP = Planar solid-state nanopore.

advantage of this configuration lies in its symmetry assessment of the electrodes.

For the measurement, DIW was loaded in two syringes connected via the through-wafer holes to both the left- and right-side reservoirs. Then, the DIW was slowly injected into the pSSNP through one of the syringe pumps to avoid the formation of air bubbles. After that, electrolytes with various KCl concentrations (5, 10, 50, 100, 500 mM and 1 M) were injected into the two reservoirs. The only path of the ionic current was through the pSSNP, verified by symmetry tests and simulation. The resistivity of the KCl solutions was calibrated using a conductivity meter (Lab 945, Xylem Analytics Germany Sales GmbH & Co. KG). The *p*H of the electrolyte was ≈6.5. Subsequently, the syringes were dismounted and the ionic current was recorded using a patch clamp amplifier (Axopatch 200B, Molecular Device Inc.). The signals were digitalized by an Axon Digidata 1550A (Molecular Device LLC.) and recorded using the software Axon pCLAMP 10 (Molecular Device LLC.). The sampling frequency was 10 kHz with a 1 kHz four-pole Bessel low-pass filter. The entire experimental setup was placed inside a Faraday cage to shield against electromagnetic interference.

For a separate experiment, a pressure regulator was used to control the N_2 gas pressure, varying from 0 to 5 bar. The pressure is set to one side reservoir of the nanopore by connecting the outlet of the pressure regulator to both the inlet and outlet of the particular reservoir filled with KCl electrolyte, as shown in Figure 2b. Then, the ionic current was recorded when switching on and off the pressure at different levels at zero bias voltage. To avoid the influence of the transient process during the pressure build-up/fall-off, the current recording lasted for at least 5 s for each measurement. The measurement was repeated 10 times at each pressure.

For the different experiments, different samples were used but their dimensions should be very similar.

3 | Results and Discussion

Images of a pSSNP were acquired under a scanning electron microscope and they are shown in Figure 2: (c) top view of the vertically and tilted top view of the horizontally aligned SiO_2 nanowire pattern before wafer bonding (Figure 1, Step 4) and (d) sideview of the pSSNP of a rectangular cross section after wafer bonding (Figure 1, Step 6). The SiO_2 nanowire in Figure 2c defines the pSSNP cross-sectional area after its removal in BHF before wafer bonding, leveraging a nanopore with its width and height identical to the nanowire width and thickness, respectively (Figure 1, Step 5).

3.1 | Conductance of Planar Solid-State Nanopores

The conductance of these 60 nm-length pSSNPs at each electrolyte (KCl) concentration ranging from 5 mM to 1 M was extracted from their respective *I–V* curves. The measurement was performed after the baseline current became stabilized. The *I–V* characteristic in the open-pore condition was obtained by applying the bias voltage from −120 to 120 mV in steps of 10 mV, as shown in Figure 3a.

The pSSNP conductance is found to increase with KCl concentration, i.e., the electrolyte conductivity, as shown in Figure 3b. The conductance–conductivity relationship deviates from the ideal linearity as lower concentrations, confirming the well-known role played by surface conduction through the electric double layer (EDL) [22]. The width of the (approximately) square cross section of the pSSNP and the surface charge density, σ, of the pSSNP sidewall are extracted by fitting the data using a simple resistance model of a square column [23]. The extracted width of 46 nm coincides well with the directly measured value in Figure 2c. The extracted surface charge density for the ALD HfO_2 layer (Figure 1, Step 6) is -0.008 C/m^2, in agreement with our previous finding [20]. It is worth noting that although surface conductance does not dominate in nanopores of this size within the studied salt concentration range and may only introduce some uncertainties in the extraction of surface charge via model fitting, the order of magnitude of the extracted values remains reliable (see details in Figure S9 in the SI).

3.2 | Noise Characteristics of Planar Nanopores

Noise has been a critical issue for vertical SSNPs fabricated on Si substrate [2, 24, 25]. As a platform of high potential for

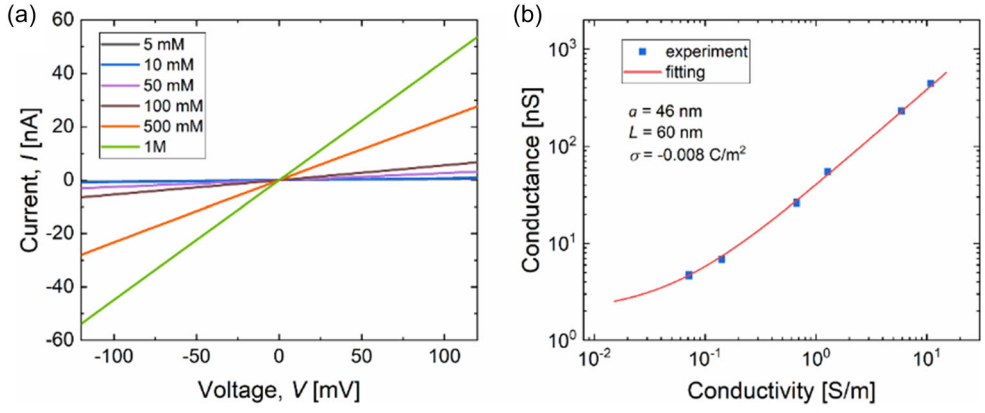

FIGURE 3 | (a) *I–V* characteristics of the 60 nm-length pSSNPs at different KCl concentrations. (b) Variation of pSSNP conductance with electrolyte conductivity from which model fitting yields the width and surface charge density of the nanopores. pSSNPs = Planar solid-state nanopores.

nanofluidic and iontronic devices, the noise characteristics of ionic current quantified as the power spectrum density (PSD), S, of pSSNPs is studied as follows. The nanopore noise can be categorized in four components in the frequency domain (i.e., $1/f$ noise, white noise, dielectric noise, and capacitive noise), each dominating in a specific frequency range and can be expressed mathematically below [2, 26]

$$S = a_1 \frac{1}{f^{\beta}} + a_2 + a_3 f + a_4 f^2 \tag{1}$$

where f is the frequency and a_{1-4} are fitting coefficients. Specifically, $a_2 = \frac{4kT}{R}$ represents thermal noise with R as nanopore resistance, k the Boltzmann constant, and T absolute temperature in Kelvin.

At low frequencies, the noise PSD is dominated by the $1/f$ noise component, i.e., the first term in Equation (1). At moderate frequencies, the dielectric noise due to dielectric losses starts becoming the major noise source, which shows a linear dependence on frequency, i.e., the third term in Equation (1). At high frequencies, the noise is dominated by the current fluctuation from the external amplifier voltage noise, i.e., the last term in Equation (1). The white noise is independent of frequency [2, 24], i.e., the second term in Equation (1). The transition region where a noise source starts to dominate could significantly vary among different experiments [2].

A typical noise PSD is shown as the black solid curve in Figure 4a. For our pSSNPs, the $1/f$ noise is well behaving and its level is comparable with those of nanopores made of other materials such as SiN_x and glass [27, 28]. However, a clear unique feature is observed in the high-frequency range >200 Hz. The noise PSD is significantly suppressed in comparison with the model curve and a plateau is observed. This feature is attributed to the low-pass filter effect arising from the parasitic capacitance and the resistance of the input–output microfluidic channels connecting to the nanopore. It is worth mentioning that with the current design and fabrication on a lossy Si substrate, the parasitic capacitance and resistance of the pSSNPs are comparably larger than those of the traditional vertical nanopore. By transferring the whole process onto a lossless substrate such as fused silica, the parasitic capacitance as well as the resulting noise at high frequencies can be dramatically suppressed or even eliminated. More details of noise analysis can be found in Supporting Note S4 in the SI. At even higher frequencies, the noise PSD rolls off around the bandwidth of the readout amplifier, i.e., 100 kHz. The noise PSD is fitted using the noise model in Equation (1) by first working on each noise component separately in its corresponding frequency range and then combining them as a complete model (red solid curve). Details about the curve fitting can be inferred in the figure caption of Figure 3b as well as found in Supporting Note S4 in the SI.

The noise characteristics were measured in different KCl concentrations ranging from 5 mM to 1 M. The resultant PSDs are shown in Figure 4b. A clear roll-off of noise is found in the high-frequency range caused by the aforementioned low-pass filter effect. The cutoff frequency increases with KCl concentration; higher concentration corresponds to lower resistance in the input–output microfluidic channels, thereby yielding a higher cutoff frequency (see Supporting Note S4 in the SI for details).

The $1/f$ noise of the nanopore increases with bias voltage (Figure S4 in the SI), which agrees with observations for other kinds of nanopores [2]. In detail, the $1/f$ noise can be further divided into three parts

$$S_{1/f} = a_1 \frac{1}{f^{\beta}} = \frac{\alpha_H}{f^{\beta}} \left(\frac{I_S^2}{N_S} + \frac{I_B^2}{N_B} \right) + \frac{a_e}{f^{\beta}} \tag{2}$$

where α_H is the Hooge parameter, I_B and I_S the current through bulk region and EDL region, respectively, and N_B and N_S the total number of conducting carriers (i.e., ions) in the bulk and EDL regions, respectively. The first two terms represent the flicker noise generated by ion number fluctuation in the nanopore bulk and in the EDL of nanopore surface; for both terms, their PSD is proportional to the square of ionic current. The third term is contributed by the modulated thermal noise of the Ag/AgCl electrodes as well as the capacitively coupled charge fluctuation from the environment. By fitting the PSD curve using the noise model in Equation (2), the contribution by the third term can be

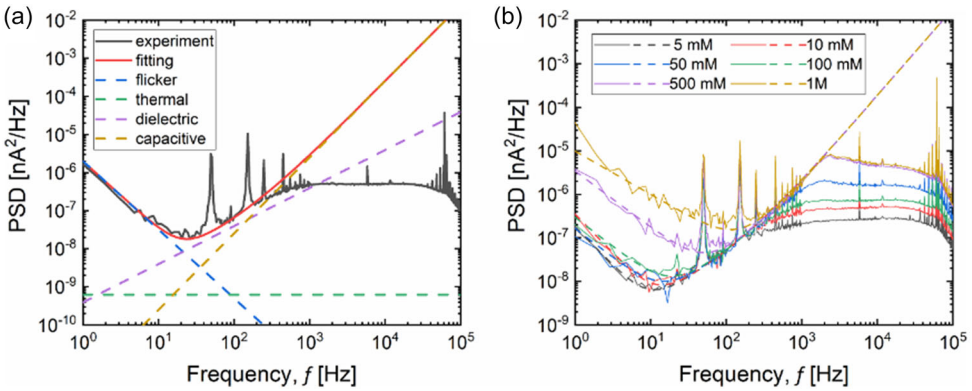

FIGURE 4 | Noise characteristics of 60 nm-length nanopore. (a) A typical noise PSD, black solid line (noisy, as expected), measured with 100 mM KCl at 100 mV bias voltage. The low-frequency range (1 Hz–200 Hz) of the PSD is fitted by the first term of Equation (1) (blue-dashed line). All other noise components in Equation (1) fitted to their respective frequency range are also displayed separately, in green-, purple-, and yellow-dashed lines. Combined, the overall fitting curve is given in red solid line. (b) Noise PSD measured with different KCl concentrations, all at 100 mV bias voltage. The solid curves are experimental data while the dashed lines are fitting results using the model in Equation (1). PSD = Power spectrum density.

extracted and its noise factor, a_e, is 1.5×10^{-7}, 3×10^{-7}, 1×10^{-9}, 1×10^{-9}, 2.5×10^{-6}, and 8×10^{-6} nA^2 for 1, 5, 10, 50, 100, 500, and 1000 mM KCl, respectively (see Supporting Note 4 in the SI). It is clear that a_e decreases and then increases with KCl concentration, which indicates that different mechanisms may be at work for this noise component. At very high KCl concentrations, the impedance of the pSSNP is small and the thermal noise from the Ag/AgCl electrodes can generate a larger current fluctuation resulting in a larger a_e. At very low KCl concentrations, however, the impedance of the nanopore is high and the environment can easily induce significant charge fluctuations in the nanopore, i.e., the capacitive coupling effect, and render a larger a_e. Thus, there appears to exist an optimized work concentration between tens to hundreds of mM. The spikes on the PSD curves at 50 Hz and its harmonic frequencies are generated by the power supply cord [29].

3.3 | Streaming current, I_{str}

Streaming current, I_{str}, is an important electrokinetic phenomenon in nanopores. It arises when a pressure gradient is applied across the nanopore with surface charge, thereby causing the water to move and drag mobile counterions in the EDL along the surface [30, 31]. The I_{str} of the pSSNPs was measured by introducing a hydraulic pressure difference, Δp, across a 60 nm-length pSSNP with a 50 mM KCl electrolyte. The schematic measurement setup can be found in Figure S5 in the SI, while the original current responses are shown in Figure S7 in the SI. The Δp causes the electrolyte with the ions to move along the pressure gradient. In EDL, there are more cations than anions as the surface charge is negative, rendering a net electric current in the EDL. By externally short-circuiting the two terminals of the pSSNP, the I_{str} is obtained. The experimental results of I_{str} versus Δp are shown in Figure 5. Obviously, the linear relationship between I_{str} and Δp faithfully follows the theoretical expression below

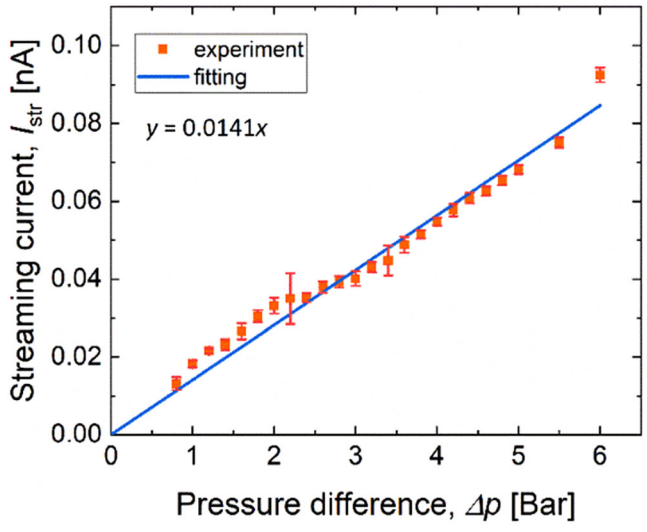

FIGURE 5 | Streaming current generated by different hydraulic pressures applied to a 60 nm-length nanopore with 50 mM KCl electrolyte. The current at each pressure was repeatedly measured 10 times.

$$I_{str} = \frac{\varepsilon_0 \varepsilon_w \zeta a^2}{\eta L} \Delta p \tag{3}$$

where ε_0 is the vacuum permittivity (8.85×10^{-12} F/m), ε_w the relative permittivity of water, a and L the feature-width and length of the pSSNP, respectively, η viscosity of water, and ζ zeta potential. From the I–V curves obtained, $a = 33$ nm and $\sigma = -0.008$ C/m^2 are extracted by assuming a square cross section (Figure S1 in the SI). By applying a linear fitting in Figure 5, ζ is calculated to be -11 mV. From the classical EDL model, the ζ of a surface with -0.008 C/m^2 charge density is -15 mV, which agrees well with the value from the I_{str} measurement (see Supporting Note S2 in the SI). The difference to the extracted cross-sectional square side length when varying KCl concentration should reflect the error in the models rather than a difference in the sample geometry. That the I_{str}–Δp relationship shows two regimes bordering around 2.5 Bar could be attributed to imperfect airtightness of the fittings and tubing in the measurement setup, especially pronounced at high pressure.

Monitoring I_{str} may offer an ultrasensitive means to complement the measurement of electrophoretic current of a nanopore. It is worth observing that I_{str} in Figure 5 is low at tens of pA. It amounts to about 2% of the electrophoretic current under similar conditions of KCl concentration and bias voltage in Figure 3a. This low percentile is in good agreement with the Dukhin number of 6% for the present experimental setup; the Dukhin number defines the ratio of surface conductance to bulk conductance number [32]. Streaming current originates from the surface conductance of a geometrically restricted channel. As such, it is directly determined by the surface conditions of the channel and not affected by the predominant bulk current driven, e.g., by the electrophoretic force in the I–V measurements. This is especially true for measurements with electrolytes of high KCl concentrations. Therefore, I_{str} measurements are usually conducted to probe surface properties such as ζ, σ, and surface chemistry in nanoscale [33]. Changes in σ can be caused by the adsorption/desorption of target molecules. Hence, monitoring I_{str} can yield useful information of the surface conditions. In this context, nanopores offer a unique advantage in sensing due to their high surface-to-volume ratio and enhanced sensitivity, which can enable applications such as real-time monitoring of surface reactions [31, 33] and biointerface characterization [34]. Moreover, I_{str} responses can be harnessed for energy conversion, forming the basis for nanofluidic salinity gradient power generation [35, 36] contributing to the design of self-powered sensors [35] and smart membranes [37].

4 | Conclusions

We have proof-of-the-concept demonstrated a novel process scheme for fabricating pSSNPs based on standard silicon technology. Because of its planar nature akin to complementary metal-oxide-semiconductor (CMOS) technology for large-scale integration of integrated circuits, this process scheme can enable seamless integration of pSSNPs with other nanofluidic elements on a single chip. Our prototype device featuring a pSSNP connected to two microscale reservoirs has been evaluated for its low-noise and streaming current characteristics, indicating its

potential for fluidic manipulations and sensing capabilities at nanoscale. Understanding the various sources of noise is both a prerequisite and a central objective of this study. Our investigation has a particular focus on the potential noise issue, especially at high frequencies because the pSSNPs are fabricated on lossy Si substrates. The pSSNP technology presented in this work is, otherwise, scalable, mechanically robust, and fully compatible with CMOS technology, thereby paving the way for high-density and high-throughput nanofluidic device integration. This advancement represents a significant step toward realizing multifunctional nanofluidic platforms that combine sensing, analysis and fluid control, thereby addressing the growing need for system-level integration in next-generation nanopore applications.

Author Contributions

Shi-Li Zhang and **Dongping Wu** conceived the idea; **Shi-Li Zhang** supervised the project; **Ngan Hoang Pham** manufactured the nanopores, assisted by **Mohammad Hadi Khaksaran** and **Won-Yong Lee**; **Mohammad Hadi Khaksaran** realized anodic bonding, supported by **Javier Cruz** and **Klas Hjört**; **Chenyu Wen** and **Won-Yong Lee** performed the measurements and simulations, with the inputs from **Ngan Hoang Pham**, **Mohammad Hadi Khaksaran**, and **Shi-Li Zhang**; **Ngan Hoang Pham**, **Chenyu Wen**, **Mohammad Hadi Khaksaran**, **Won-Yong Lee**, and **Shi-Li Zhang** analyzed the data; **Ngan Hoang Pham**, **Chenyu Wen**, and **Shi-Li Zhang** wrote the manuscript. All authors commented on the manuscript.

Acknowledgments

This study was partially financed by the Swedish Research Council (2022–03222). We acknowledge Myfab Uppsala for providing facilities and experimental support, with the support of Myfab as a national research infrastructure by the Swedish Research Council (2019–00207).

Funding

This study was partially financed by the Swedish Research Council (2022-03222).

References

1. C. Wen and S.-L. Zhang, "Fundamentals and Potentials of Solid-State Nanopores," *Journal of Physics D: Applied Physics* 54, no. 2 (2020): 023001, https://doi.org/10.1088/1361-6463/ababce.

2. C. Wen, S. Zeng, K. Arstila, et al., "Generalized Noise Study of Solid-State Nanopores at Low Frequencies," *ACS Sensors* 2, no. 2 (2017): 300–307, https://doi.org/10.1021/acssensors.6b00826.

3. Y. Yao, C. Wen, N. H. Pham, and S.-L. Zhang, "On Induced Surface Charge in Solid-State Nanopores," *Langmuir: The ACS Journal of Surfaces and Colloids* 36, no. 30 (2020): 8874–8882, https://doi.org/10.1021/acs.langmuir.0c01189.

4. D. G. Haywood, Z. D. Harms, and S. C. Jacobson," Electroosmotic Flow in Nanofluidic Channels," *Analytical Chemistry* 86, no. 22 (2014): 11174–11180, https://doi.org/10.1021/ac502596m.

5. ScienceDirect Topics. Low-Grade Heat Source - An Overview. (Accessed Jan 1, 2024). https://www.sciencedirect.com/topics/engineering/low-grade-heat-source.

6. W. Q. Chen, A. P. Jivkov, and M. Sedighi, "Thermo-Osmosis in Charged Nanochannels: Effects of Surface Charge and Ionic Strength," *ACS Applied Materials and Interfaces* 15, no. 28 (2023): 34159–34171, https://doi.org/10.1021/acsami.3c02559.

7. P. Ramirez, S. Portillo, J. Cervera, et al., "Neuromorphic Responses of Nanofluidic Memristors in Symmetric and Asymmetric Ionic Solutions," *The Journal of Chemical Physics* 160, no. 4 (2024): 044701, https://doi.org/10.1063/5.0188940.

8. Z. Wang, L. Wang, M. Nagai, L. Xie, M. Yi, and W. Huang, "Nanoionics-Enabled Memristive Devices: Strategies and Materials for Neuromorphic Applications," *Advanced Electronic Materials* 3, no. 7 (2017): 1600510, https://doi.org/10.1002/aelm.201600510.

9. M. Tsutsui, K. Yokota, Y. He, and T. Kawai, "Ionic Signal Amplification of DNA in a Nanopore," *Small Methods* 6, no. 11 (2022): 2200761, https://doi.org/10.1002/smtd.202200761.

10. S. Zeng, C. Wen, P. Solomon, S.-L. Zhang, and Z. Zhang, "Rectification of Protein Translocation in Truncated Pyramidal Nanopores," *Nature Nanotechnology* 14, no. 11 (2019): 1056–1062, https://doi.org/10.1038/s41565-019-0549-0.

11. N. H. Pham, Y. Yao, C. Wen, et al., "Self-Limited Formation of Bowl-Shaped Nanopores for Directional DNA Translocation," *ACS Nano* 15, no. 11 (2021): 17938–17946, https://doi.org/10.1021/acsnano.1c06321.

12. M. Zhang, C. Ngampeerapong, D. Redin, A. Ahmadian, I. Sychugov, and J. Linnros, "Thermophoresis-Controlled Size-Dependent DNA Translocation through an Array of Nanopores," *ACS Nano* 12, no. 5 (2018): 4574–4582.

13. T. Deng, M. Li, Y. Wang, and Z. Liu, "Development of Solid-State Nanopore Fabrication Technologies," *Science Bulletin* 60, no. 3 (2015): 304–319, https://doi.org/10.1007/s11434-014-0705-8.

14. H. Liu, Q. Zhou, W. Wang, F. Fang, and J. Zhang, "Solid-State Nanopore Array: Manufacturing and Applications.," *Small* 19, no. 6 (2023): 2205680, https://doi.org/10.1002/smll.202205680.

15. K. Lee, K.-B. Park, H.-J. Kim, et al., "Recent Progress in Solid-State Nanopores," *Advanced Materials* 30, no. 42 (2018): 1704680, https://doi.org/10.1002/adma.201704680.

16. C. Wen, S. Zeng, S. Li, Z. Zhang, and S.-L. Zhang, "On Rectification of Ionic Current in Nanopores," *Analytical Chemistry* 91, no. 22 (2019): 14597–14604, https://doi.org/10.1021/acs.analchem.9b03685.

17. M. Zhang, Z. D. Harms, T. Greibe, C. A. Starr, A. Zlotnick, and S. C. Jacobson, "In-Plane, In-Series Nanopores With Circular Cross Sections for Resistive-Pulse Sensing," *ACS Nano* 16, no. 5 (2022): 7352–7360, https://doi.org/10.1021/acsnano.1c08680.

18. P. Kondylis, J. Zhou, Z. D. Harms, et al., "Nanofluidic Devices With 8 Pores in Series for Real-Time, Resistive-Pulse Analysis of Hepatitis B Virus Capsid Assembly.," *Analytical Chemistry* 89, no. 9 (2017): 4855–4862, https://doi.org/10.1021/acs.analchem.6b04491.

19. S. Shivanka, F. Shiri, M. Chibuike, et al., "Insights on Using Plastic-Based Dual in-Plane Nanopore Sensors for Differentiation and Shape Determinations of Single Protein Molecules," *Scientific Reports* 15, no. 1 (2025): 13742, https://doi.org/10.1038/s41598-025-96232-y.

20. S. Li, S. Zeng, C. Wen, et al., "Dynamics of DNA Clogging in Hafnium Oxide Nanopores," *The Journal of Physical Chemistry. B* 124, no. 51 (2020): 11573–11583, https://doi.org/10.1021/acs.jpcb.0c07756.

21. C. Wen, E. Bertosin, X. Shi, C. Dekker, and S. Schmid, "Orientation-Locked DNA Origami for Stable Trapping of Small Proteins in the Nanopore Electro-Osmotic Trap," *Nano Letters* 23, no. 3 (2023): 788–794, https://doi.org/10.1021/acs.nanolett.2c03569.

22. D. Stein, M. Kruithof, and C. Dekker, "Surface-Charge-Governed Ion Transport in Nanofluidic Channels," *Physical Review Letters* 93, no. 3 (2004): 035901, https://doi.org/10.1103/PhysRevLett.93.035901.

23. C. Wen, Z. Zhang, and S.-L. Zhang, "Physical Model for Rapid and Accurate Determination of Nanopore Size via Conductance Measurement," *ACS Sensors* 2, no. 10 (2017): 1523–1530, https://doi.org/10.1021/acssensors.7b00576.

24. J. D. Uram, K. Ke, and M. Mayer, "Noise and Bandwidth of Current Recordings From Submicrometer Pores and Nanopores," *ACS Nano* 2, no. 5 (2008): 857–872, https://doi.org/10.1021/nn700322m.

25. H. K. Gatty, N. X. Chung, M. Zhang, I. Sychugov, and J. Linnros, "Fabrication of Individual Solid-State Nanopores for Sensing Single DNAs," *Nanotechnology* 31, no. 35 (2020): 355505, https://doi.org/10.1088/1361-6528/ab9474.

26. V. Tabard-Cossa, D. Trivedi, M. Wiggin, N. N. Jetha, and A. Marziali, "Noise Analysis and Reduction in Solid-State Nanopores," *Nanotechnology* 18, no. 30 (2007): 305505, https://doi.org/10.1088/0957-4484/18/30/305505.

27. L. J. Steinbock, R. D. Bulushev, S. Krishnan, C. Raillon, and A. Radenovic, "DNA Translocation Through Low-Noise Glass Nanopores," *ACS Nano* 7, no. 12 (2013): 11255–11262, https://doi.org/10.1021/nn405029j.

28. A. Fragasso, S. Schmid, and C. Dekker, "Comparing Current Noise in Biological and Solid-State Nanopores," *ACS Nano* 14, no. 2 (2020): 1338–1349, https://doi.org/10.1021/acsnano.9b09353.

29. D. Zhang, X. Gao, S. Chen, et al., "An Ion-Gated Bipolar Amplifier for Ion Sensing With Enhanced Signal and Improved Noise Performance," *Applied Physics Letters* 105 (2014): 082102, https://doi.org/10.1063/1.4894240.

30. Y.-T. Chen and J.-P. Hsu, "Pressure-Driven Power Generation and Ion Separation Using a Non-Uniformly Charged Nanopore," *Journal of Colloid and Interface Science* 607 (2022): 1120–1130, https://doi.org/10.1016/j.jcis.2021.09.055.

31. T.-Y. Tsou and J.-P. Hsu, "Pressure-Driven Ion Separation Through a pH-Regulated Cylindrical Nanopore," *Journal of Membrane Science* 604 (2020): 118073, https://doi.org/10.1016/j.memsci.2020.118073.

32. C. Wen and S.-L. Zhang, "On Current Blockade Upon Analyte Translocation in Nanopores," *Journal of Applied Physics* 129 (2021): 064702, https://doi.org/10.1063/5.0035113.

33. S. S. Sahu, M. T. Gevari, Á. Nagy, et al., "Profiling of Extracellular Vesicles Using Streaming Current and Sequential Electrostatic Labeling," *Biosensors and Bioelectronics* 227 (2023): 115142, https://doi.org/10.1016/j.bios.2023.115142.

34. S. Buyukdagli, R. Blossey, and T. Ala-Nissila, "Ionic Current Inversion in Pressure-Driven Polymer Translocation Through Nanopores," *Physical Review Letters* 114, no. 8 (2015): 088303, https://doi.org/10.1103/PhysRevLett.114.088303.

35. D. Manikandan, S. Karishma, M. Kumar, and P. K. Nayak, "Salinity Gradient Induced Blue Energy Generation Using Two-Dimensional Membranes," *NPJ 2d Materials and Applications* 8, no. 1 (2024): 1–19, https://doi.org/10.1038/s41699-024-00486-5.

36. L. Wang, Z. Wang, S. K. Patel, S. Lin, and M. Elimelech, "Nanopore-Based Power Generation From Salinity Gradient: Why it is Not Viable," *ACS Nano* 15, no. 3 (2021): 4093–4107, https://doi.org/10.1021/acsnano.0c08628.

37. S. Chae, H. Kim, J. Gi Hong, et al., "Clean Power Generation From Salinity Gradient Using Reverse Electrodialysis Technologies: Recent Advances, Bottlenecks, and Future Direction," *Chemical Engineering Journal* 452 (2023): 139482, https://doi.org/10.1016/j.cej.2022.139482.

Supporting Information

Additional supporting information can be found online in the Supporting Information section.